Hindawi
Advances in Civil Engineering
Volume 2024, Article ID 7170963, 13 pages
https://doi.org/10.1155/2024/7170963

Research Article

Experimental Study on the Boundary Reflection Effect of Stress Wave Propagation Based on the Newly Developed Test Apparatus

Jian Wu,[1,2,3] Yan-Tang Gao,[1,2] Shao-Hui Tang,[4] Zhi-Quan Zeng,[1,2] Ning Miao,[1,2] Yun-Zhi Zhong,[1] Lei Huang,[1,2] and Quan-Sheng Liu[4]

[1]*Power China Huadong Engineering Corporation Limited, Hangzhou 311122, China*
[2]*Hangzhou Huadong Underground Engineering Intelligent Equipment Research Institute Corporation Limited, 311122, Hangzhou, China*
[3]*Zhejiang Engineering Research Center of Green Mine Technology and Intelligent Equipment, 311122, Hangzhou, China*
[4]*Key Laboratory of Safety for Geotechnical and Structural Engineering of Hubei Province, School of Civil Engineering, Wuhan University, 430072, Wuhan, China*

Correspondence should be addressed to Shao-Hui Tang; tangshaohui0723@163.com

Received 24 February 2024; Revised 12 April 2024; Accepted 22 April 2024; Published 30 April 2024

Academic Editor: Shiming Wang

There is a ubiquitous boundary reflection effect of stress wave propagation in the indoor experimental studies. It is critical to improve the validity of waveform data by optimizing boundary materials to absorb reflection waves. In the present study, a calculation method for the optimal wave impedance of boundary materials was proposed based on the transmission and reflection principle of one-dimensional stress waves at the interface of different media. By using the calculation method, the optimal wave impedance value of the boundary material was obtained. A one-dimensional stress wave propagation test apparatus was developed for exploring the improvement effect of absorbing materials on the boundary reflection effect. One-dimensional stress wave propagation experimental studies in the complete red sandstone samples were carried out by setting various boundary absorbing materials such as pine pad, rubber pad, and steel pad. The results indicated that the experimental test results were consistent with the theoretical calculation results. In the stress wave propagation tests, the optimal wave impedance value of the boundary material was 1.12×10^6 kg/m^2·s. When the pine pads were used as boundary absorbing materials, the suppression effect of boundary reflection effects is relatively the best. The present study provides references for analyzing the characteristics and mechanism of stress wave propagation and attenuation.

1. Introduction

With the increasing demands for public infrastructure and resource mining, dynamic disturbances such as blasting excavation, mine exploitation, rock burst, and advanced detection often occur in deep rock masses [1–9]. The dynamic disturbances will crack rock mass and release elastic energy, which is released and propagated as stress waves (the propagation of variation in stress or strain states in the form of waves in the medium). According to different classification methods, they are divided into *P* waves, *S* waves, elastic waves, plastic waves, viscoelastic waves, etc. [7, 10–12]. The verification of the propagation pattern and the attenuation mechanism of stress waves in rock masses is important for determining rock mass stability, estimating focal energy and improving seismic resistance [13–20]. Preliminary literature surveys indicate that the theoretical analysis, experimental test, and field study on the propagation attenuation patterns of stress waves have achieved promising achievements [16, 21–30]. Due to the complex distribution of natural joint cracks, engineering rock mass mechanics parameters are difficult to accurately measure [26, 31, 32]. Theoretical analysis such as the continuum medium method, discontinuous medium method, and two-phase medium method cannot accurately reveal the propagation attenuation patterns of stress waves in the complex engineering rock masses [33–35].

Field studies of stress wave excitation, propagation, and attenuation patterns are the same as those in engineering

practice [36, 37]. The seismic source is directly excited in the rock masses of underground engineering [38, 39]. The waveform signals at different propagation distances are collected to study the attenuation patterns of stress wave propagation [40–42]. For instance, Zhang et al. [43] conducted field studies at Xincun Coal Mine and analyzed the attenuation characteristics of microseismic energy propagation to classify potential rock burst zones. Jiang et al. [44] studied the propagation attenuation of blasting vibration based on Daye Iron Mine and proposed a prediction model to evaluate the potential risks of blasting vibrations. Wu et al. [40] explored attenuation patterns of the pendulum impact signal at a deep tunnel and established the relationship between the energy attenuation coefficient and the wave impedance of rock mass to predict the potential risk of rock bursts in mudstone. However, the in situ stress wave propagation test is expensive and poorly reproducible. The test results are prone to be affected by the geological site conditions [9, 45, 46].

The experimental test can not only validate theoretical analysis but also guide field applications [22, 25, 47]. It was widely used to study the attenuation characteristics of stress wave propagation due to the advantages of good operability, high repeatability, and controllable conditions. For instance, Tian et al. [48] explored the effect of structural surfaces on particle vibration velocity and found that the stress wave amplitude attenuates more significantly as the structural surface increases. Zou et al. [49] monitored the waveform data at different parts of the rock samples and studied the seismic response pattern of a joint rock with an oblique incidence of plane *P* waves. Liu et al. [50] proposed a Split Shear Plates model based on the newly developed test apparatus and investigated the influence of the fill thickness, particle size, and normal stress on wave propagation. Li et al. [51] studied the wave propagation and attenuation pattern in fractured rock mass and revealed the effects of crack number, crack angles, and confining pressure on the attenuation patterns of the elastic wave amplitude.

The above experimental tests did not consider the boundary reflection effect of stress waves. To the best of our knowledge, there is still a lack of experimental study on boundary reflection of stress wave propagation. When the physical percussion is used to excite a seismic source, the reflected wave propagates to the monitoring point, which will cause superposition and interference with the original waveform. It is difficult for the signal to accurately reflect the propagation attenuation pattern of the stress wave in the rock medium. It means that the boundary reflection will affect the reliability of test data. How to reduce the disturbance of boundary reflection on test data is an urgent problem to be solved in the stress wave propagation test.

In the present study, the boundary reflection effect of stress wave propagation was investigated by the theoretical derivation and the experimental test. First, a calculation model of the optimal wave impedance of the boundary material was proposed based on the transmission and reflection principle of a one-dimensional stress wave (the stress wave propagates in a one-dimensional rod). Second, a new test apparatus was developed to study stress wave propagation and attenuation patterns. Experimental tests in complete red sandstone samples were carried out to analyze the boundary reflection effects of various boundary absorbing materials on stress waves. The experimental results were compared and validated with the theoretical results so as to select the appropriate boundary absorbing materials to improve the boundary reflection effect of stress waves.

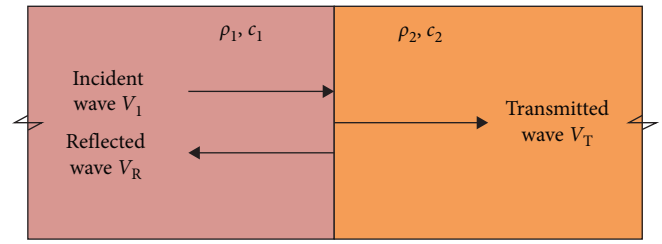

FIGURE 1: The transmission and reflection of one-dimensional *P*-wave.

2. Transmission and Reflection of *P*-Wave at the Media Interface

As shown in Figure 1, when the incident stress wave V_I propagates from medium 1 to medium 2 perpendicular to the interface, the wave impedance changes from $Z_1 = \rho_1 \cdot c_1$ to $Z_2 = \rho_2 \cdot c_2$. The transmitted wave V_T and the reflected wave V_R will generate and propagate into two media. As long as medium 1 and medium 2 are in contact with each other, the stress and velocity of adjacent particles are equal after the transflection effect [52]. Details can be expressed as Equation (1).

$$\begin{cases} \sigma_I + \sigma_R = \sigma_T \\ V_I + V_R = V_T \end{cases}. \tag{1}$$

According to the conservation of wavefront momentum discussed by Wang [52], $\sigma_I = Z_1 V_I$, $\sigma_R = -Z_1 V_R$, and $\sigma_T = Z_2 V_T$. Then, Equation (2) can be obtained:

$$\begin{cases} V_R = \dfrac{Z_1 - Z_2}{Z_1 + Z_2} \cdot V_I = R \cdot V_I \\ V_T = \dfrac{2Z_1}{Z_1 + Z_2} \cdot V_I = T \cdot V_I \end{cases}, \tag{2}$$

$$\begin{cases} \sigma_R = \dfrac{Z_2 - Z_1}{Z_1 + Z_2} \cdot \sigma_I = -R \cdot \sigma_I \\ \sigma_T = \dfrac{2Z_2}{Z_1 + Z_2} \cdot \sigma_I = nT \cdot \sigma_I \end{cases}, \tag{3}$$

where R is the reflection coefficient at the interface between medium 1 and medium 2, and T is the transmission coefficient at the interface, which can be calculated from the wave impedance values of two media. It satisfies $T = 1 + R$.

According to Equation (3), the propagation direction of the transmitted wave is consistent with that of the incident wave, and the direction of particle motion velocity is the same [52]. However, the propagation direction of the reflection

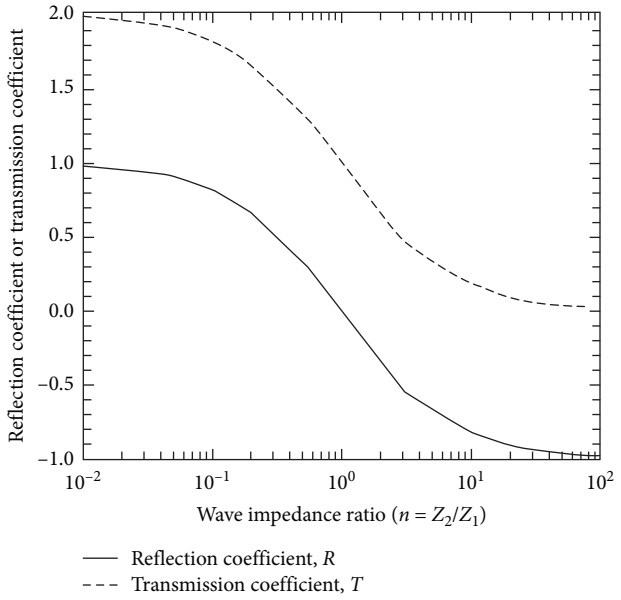

FIGURE 2: The relationship between reflection coefficient and transmission coefficient with wave impedance ratio n.

wave is opposite to that of the incident wave. Particle motion velocity depends on the relative magnitude of the wave impedance. When the ratio of the wave impedance of medium 2 to that of medium 1 is n ($n = Z_2/Z_1$), the variation in the reflection coefficient and transmission coefficient with the wave impedance ratio is shown in Figure 2.

According to the variation in the wave impedance ratio of different media [52–54], there are three conditions need to be discussed:

(1) When $Z_1 > Z_2$, the stress wave propagates from the "hard" medium to the "soft" medium ($\sigma_R\sigma_I < 0$ and $\sigma_T < \sigma_I$). The stress disturbance σ_R and the stress perturbation σ_I are in the opposite direction, while the stress perturbation σ_T and the stress perturbation σ_I are in the same direction, and their amplitudes are weaker than the incident perturbation. When $V_R < V_I$ and $V_T > V_I$, the particle velocity V_R and the particle velocity V_I are in the same direction, but the amplitude is greater than that of the incident wave. The particle velocity V_T is in the same direction as the particle velocity V_I, but the amplitude of the former is greater than that of the latter.

When Z_2 approaches zero, the stress wave is reflected at the free end ($\sigma_R = -\sigma_I$ and $\sigma_T = 0$). The stress disturbance σ_R at the free end and the stress disturbance σ_I are opposite in directions and equal in amplitude. The force at the free end is zero, which satisfies the boundary conditions. When $V_R = V_I$ and $V_T = 2V_I$, the particle velocity V_R and the particle velocity V_I are the same in direction and amplitude. The particle velocity V_T at the free end is twice that of the incident wave.

(2) When $Z_1 < Z_2$, the stress wave propagates from the "soft" medium to the "hard" medium ($\sigma_R < \sigma_I$ and $\sigma_T > \sigma_I$). The stress disturbance σ_R is in the same direction as the stress disturbance σ_I, and the amplitude is smaller than that of the incident disturbance. The stress disturbance σ_T is in the same direction as the stress disturbance σ_I, and the amplitude of the former is larger than that of the incident disturbance. When $V_R \cdot V_I < 0$ and $V_T < V_I$, the particle velocity V_R and the particle velocity V_I are in the opposite direction. The particle velocity V_T and the particle velocity V_I are in the same direction, but their amplitudes are smaller than that of the incident wave.

When Z_2 approaches infinity, the stress wave is reflected at the fixed end ($\sigma_R = \sigma_I$ and $\sigma_T = 2\sigma_I$). The stress disturbance σ_R at the fixed end and the stress disturbance σ_I are the same in direction and amplitude. The total internal force at the fixed end is twice that of the incident wave disturbance. When $V_R = -V_I$ and $V_T = 0$, the particle velocity V_R and the particle velocity V_I are in opposite directions and have the same amplitude. Particle motion velocity at the fixed end is zero, which satisfies the boundary conditions.

(3) When $Z_1 = Z_2$, the stress wave propagates through two media with same wave impedances. The stress wave propagates into medium 2 without a reflection wave under the premise that the interfaces are in close contact and do not deform during the propagation process of stress waves.

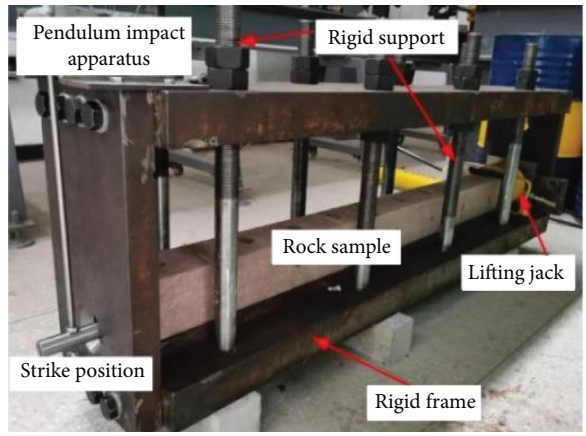

FIGURE 3: Stress wave propagation attenuation test apparatus.

In the experimental test, due to the limitation of specimen size, the stress wave generates reflected waves at the boundary. It causes the superimposed interference of the incident wave and the reflected wave. Hence, it is necessary to reduce the disturbance of reflected waves. The boundary reflection effect and the wave impedance matching of boundary materials will be discussed in the following sections.

3. Boundary Reflection Effect of Stress Wave Propagation Test

3.1. Stress Wave Propagation Test Apparatus. In order to study the attenuation patterns of stress wave propagation in rock under loading, a stress wave propagation attenuation test apparatus was developed (Figure 3). The test apparatus consists of

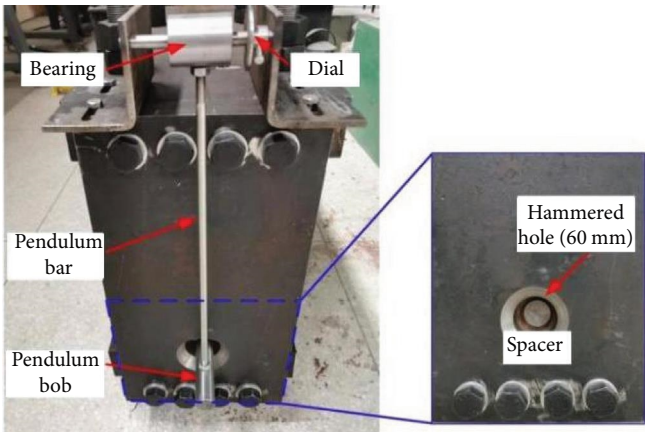

Figure 4: Pendulum impact module.

the rigid compression frame, pendulum impact, and horizontal loading module. The rigid frame with the structural dimensions of 1,850 mm × 500 mm × 500 mm (length × width × height) is composed of four steel plates with a thickness of 50 mm. It is used to bear the reaction force generated by the horizontal jack loading to ensure the overall stiffness of the test apparatus. The pendulum impact module is mainly composed of the center bearing, pendulum rod, pendulum, and dial. The pendulum bar is made of slender iron with a length of 500 mm and a diameter of 10 mm. The upper end of the pendulum bar is connected by threads. The pendulum bob is 110 mm in length and 30 mm in diameter (0.632 kg). The dial is used to read the swing angle of the pendulum bob (Figure 4). The horizontal loading module used a manual hydraulic oil pump to control the jack to apply the horizontal load. The applicable load range is 0–100 MPa, which satisfies the loading demands of the stress wave propagation test.

3.2. Specimen Preparation. The rock specimen used in the stress wave attenuation test was long columnar red sandstone from Ezhou, Hubei Province. The dimensions of length, width, and height were 1,500 mm × 120 mm × 120 mm (Figure 5(a)), and the aspect ratio was 12.5. The two end sections were flat and parallel to each other. When the rock specimen aspect ratio is greater than 10, the propagation path of the point wave source in the long columnar can be approximated as a one-dimensional stress wave. To obtain the physical and mechanical parameters of the red sandstone, five standard rock specimens (50 mm in diameter and 100 mm in height) were drilled from a red sandstone rock block (Figure 5(b)). The uniaxial compression tests were performed on a hydraulic testing machine RMT-301 (Figure 5(c)). The damaged rock specimens after the uniaxial compression test are shown in Figure 5(d). The physical and mechanical parameters are listed in Table 1. The corresponding stress–strain curves are shown in Figure 6.

3.3. Stress Wave Propagation Test under Free Boundary Conditions. Figure 7 shows the schematic diagram of experimental tests on the stress wave propagation attenuation in an intact rock specimen under free boundary conditions, which displays the spatial relationship between the rock specimen, test apparatus, and sensor arrangement. The rock specimen

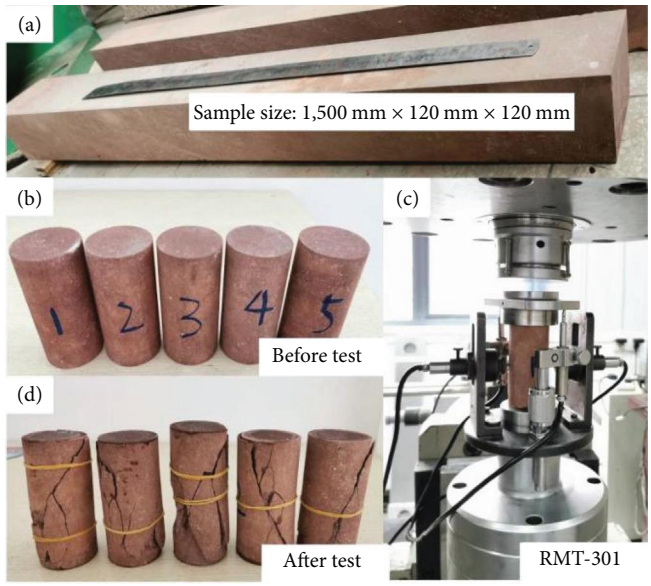

Figure 5: Uniaxial compression test for red sandstone specimens: (a) columnar red sandstone, (b) specimens before test, (c) specimens after test, and (d) uniaxial compression test.

was arranged longitudinally in the rigid frame. A polyethylene plastic film was added to the contact face between the rock specimen and the rigid frame to reduce the friction to improve the boundary contact condition and reduce the disturbance of external stress waves. The stress wave is excited by raising the pendulum bob to a certain height and then falling freely to hit the rock specimen. In order to improve the repeatability and reliability of stress waves, a metal pad was installed at the striking point to avoid partial fracture of the rock specimen caused by hammering. The acceleration sensor was closely attached to the rock specimen surface. The attachment position should be polished with sandpaper, and then, the sensor was attached to the upper surface of the rock specimen using a high viscosity quick-drying adhesive with good work performance. The acceleration signals at various propagation distances were collected. The monitoring line was located at the midline on the upper surface of the rock specimen. The distance between sensor 1# and the left end was 200 mm, and that between sensor 6# and the right end was 300 mm. The six acceleration sensors were evenly distributed at intervals of 200 mm. Five stress wave events F-1, F-2, F-3, F-4, and F-5 with different initial amplitudes were excited by changing the pendulum height. The waveform energy of the sensor signal was calculated according to Equation (4):

$$E = \frac{1}{2}\Delta m \int_{t_s}^{t_e} v^2(t)dt, \tag{4}$$

where E is the energy of signal waveform, Δm is the mass of unit particle, t_s is the start time of velocity to time curve, t_e is the end time of velocity to time curve, and $v(t)$ is the velocity to time curve.

Table 1: Physical and mechanical parameters of red sandstone.

Parameters	Uniaxial compressive strength, σ_c (MPa)	Elastic modulus, E (GPa)	Poisson's ratio, μ	Wave speed, v (m/s)	Density, ρ (g/cm^3)
Values	40.89	9.26	0.21	3,209	2.35

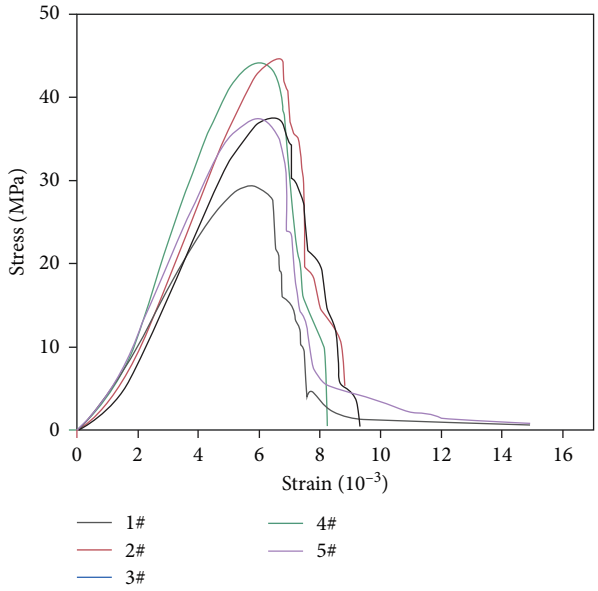

Figure 6: The stress–strain curves of red sandstone.

The stress wave attenuation tests in the complete rock specimens were conducted. Figure 8 shows the variation in the stress wave energy with the propagation distance under free boundary conditions. Taking event F-5 as an example, as the propagation distance increased, the energy of waveforms received by sensors 1# to 6# was 5.36, 4.84, 5.33, 4.16, 4.33, and 3.74 (10^{-6} J), respectively. The energy of stress waves received by sensors #3 and #5 was higher than that of the signal received by the previous sensor. Five striking events showed similar characteristics.

Figure 9 is the acceleration time–history curves received by acceleration sensors 1# to 6# during the event F-5. The acceleration waveform was integrated to obtain the velocity time–history curve (Figure 10). The acceleration waveform of event F-5 lasted approximately 10 ms. After reaching the initial peak, there was an obvious multiple peak phenomenon. It is related to the waveform superposition phenomenon caused by the reflected wave peaks at the boundary. This is also the reason for the anomaly in the stress wave energy attenuation pattern in Figure 8.

4. Calculation Model of the Optimal Wave Impedance for Boundary Material

In order to reduce the reflection effect of stress waves at the free boundary, it is necessary to select an appropriate medium material to absorb the reflected wave. Based on the transmission and reflection principles of stress waves at the boundary of different media, a calculation model with optimal wave impedance matching was developed (Figure 11). In order to simplify the calculation process, only the transmission and reflection effects of one-dimensional stress waves among the three media were considered. The medium a on the left was the red sandstone sample, with a wave impedance of $Z_a = \rho_a \times c_a = 2{,}960 \times 2{,}350 = 6.96 \times 10^6$ kg/m^2·s. The medium c on the right was a steel block, with a wave impedance of $Z_c = \rho_c \times c_c = 7{,}900 \times 5{,}200 = 41.08 \times 10^6$ kg/m^2·s. The medium b in the middle was the wave-absorbing material, and the wave impedance Z_b was required to be determined.

When the incident wave V_{I} propagated from medium a to medium b, the first transmission and reflection occurred at interface I. During this process, the reflected wave V_{R1} and transmitted wave V_{T1} were generated:

$$\begin{cases} V_{\mathrm{R1}} = \dfrac{Z_a - Z_b}{Z_a + Z_b} \cdot V_{\mathrm{I}} \\ V_{\mathrm{T1}} = \dfrac{2Z_a}{Z_a + Z_b} \cdot V_{\mathrm{I}} \end{cases}. \tag{5}$$

When the transmitted wave V_{T1} propagated from medium b to medium c, the second transmission and reflection occurred at interface II. In this process, the reflected wave V_{R2} and transmitted wave V_{T2} were generated:

$$\begin{cases} V_{\mathrm{R2}} = \dfrac{Z_b - Z_c}{Z_b + Z_c} \cdot V_{\mathrm{TI}} \\ V_{\mathrm{T2}} = \dfrac{2Z_b}{Z_b + Z_c} \cdot V_{\mathrm{TI}} \end{cases}. \tag{6}$$

When the reflected wave V_{R2} propagated from medium b to medium a, the third transmission and reflection occurred at interface I. The reflected wave V_{R3} and transmitted wave V_{T3} were generated in this process:

$$\begin{cases} V_{\mathrm{R3}} = \dfrac{Z_b - Z_a}{Z_b + Z_a} \cdot V_{\mathrm{R2}} \\ V_{\mathrm{T3}} = \dfrac{2Z_b}{Z_b + Z_a} \cdot V_{\mathrm{R2}} \end{cases}. \tag{7}$$

Additionally, multiple transmissions and reflections of stress waves occurred at interfaces I and II. According to Figure 11, the left-traveling stress waves reflected back into medium a were denoted as V_L (including V_{R1}, V_{T3}, and V_{T5}) and illustrated in Equation (8). Substituting Equations (5)–(7) into Equation (8), the expression of the left-traveling stress waves V_L is shown in Equations (9) and (10):

$$V_L = V_{\mathrm{R1}} + V_{\mathrm{T3}} + V_{\mathrm{T5}} + \cdots, \tag{8}$$

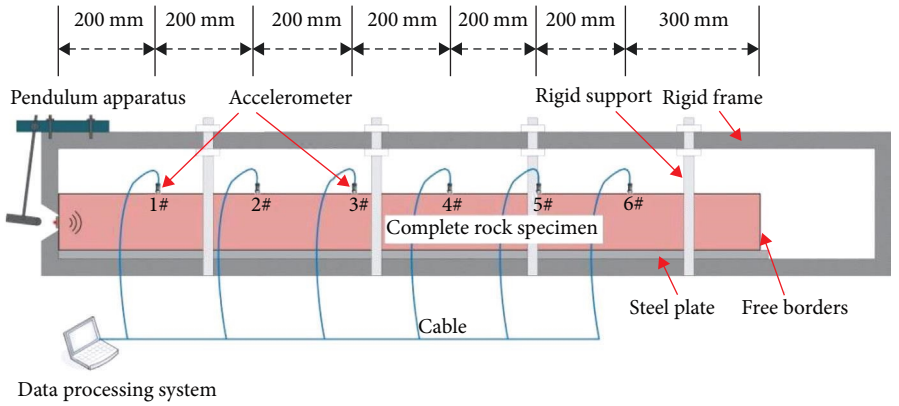

Figure 7: The stress wave attenuation test in complete rock specimen (free boundary condition).

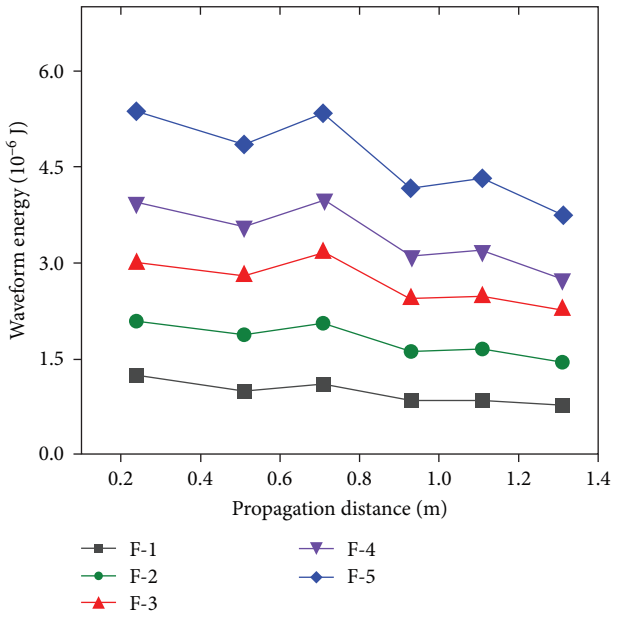

Figure 8: Variation in stress wave energy with propagation distance under free boundary condition.

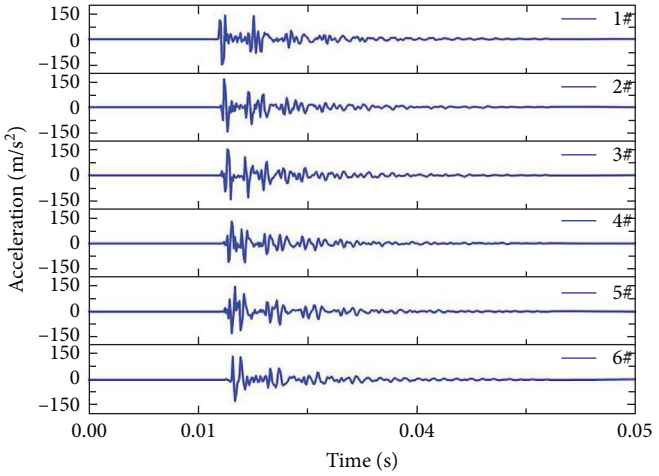

Figure 9: Time–history curves of acceleration from 1# to 6# (event F-5).

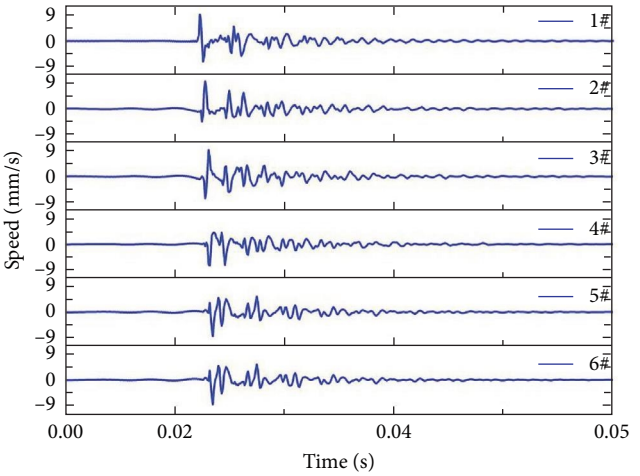

Figure 10: Time–history curves of velocity from 1# to 6# (event F-5).

$$V_L = \frac{Z_a - Z_b}{Z_a + Z_b} \cdot V_{\mathrm{I}} + \frac{2Z_b}{Z_b + Z_a} \cdot V_{\mathrm{R2}} + \frac{2Z_b}{Z_b + Z_a} \cdot V_{\mathrm{R4}} + \cdots, \tag{9}$$

$$V_L = \left(\frac{Z_a - Z_b}{Z_a + Z_b} + \frac{2Z_b}{Z_b + Z_a} \cdot \frac{Z_b - Z_c}{Z_b + Z_c} \cdot \frac{2Z_a}{Z_a + Z_b} + \frac{2Z_b}{Z_b + Z_a} \cdot \frac{Z_b - Z_c}{Z_b + Z_c} \cdot \frac{Z_b - Z_a}{Z_b + Z_a} \cdot \frac{Z_b - Z_c}{Z_b + Z_c} \cdot \frac{2Z_a}{Z_a + Z_b} + \cdots \right) \cdot V_{\mathrm{I}}. \tag{10}$$

As the number of transmissions and reflections increases, the amplitude of the left-traveling stress wave that is reflected back to the rock specimen decreases. In order to simplify the calculation, only the first three terms in the expression for V_L are selected, and the magnitude of the subsequent left-traveling wave is ignored. Then, the left-traveling wave in Equation (8) can be expressed as Equation (11):

$$V_L = V_{\mathrm{R1}} + V_{\mathrm{T3}} + V_{\mathrm{T5}}. \tag{11}$$

The variation in V_L/V_{I} with the wave impedance Z_b is shown in Figure 12 (the positive value represents that the

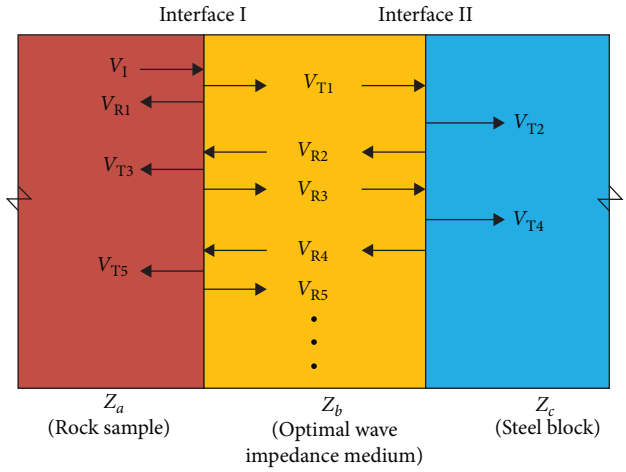

Figure 11: Transmission and reflection of stress waves in three media.

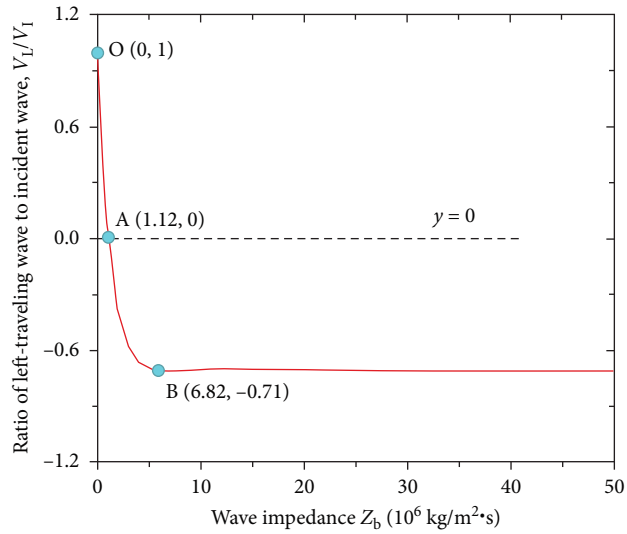

Figure 12: Variation in the left-travel wave with wave impedance value of b-medium.

particle vibration directions of the left-traveling wave and the incident wave are in the same direction. The negative value represents that the left-traveling wave and the incident wave of the particle vibrate are in the opposite direction). When the wave impedance Z_b increases from 0 to 1.12×10^6 kg/m^2·s, the V_L/V_I ratio curve decreases rapidly. The left-traveling wave gradually weakens. When the wave impedance is $Z_b = 1.12 \times 10^6$ kg/m^2·s, the left-traveling wave is zero. Point A represents the optimal wave impedance value in this conditions. As the wave impedance Z_b increases from 1.12×10^6 to 6.82×10^6 kg/m^2·s, the V_L/V_I ratio increases from 0 to −0.71. The amplitude of the left-traveling wave gradually increases. When the wave impedance Z_b continues to increase, the V_L/V_I ratio gradually stabilizes. In this case, the optimal wave impedance of the boundary absorbing material is $Z_{op} = 1.12 \times 10^6$ kg/m^2·s.

5. The Influence of Boundary Absorbing Material on Stress Wave Propagation

The boundary absorbing material should satisfy two requirements. First, its internal structure should be porous. When the stress wave propagates in a porous structure, the complex scattering effect results in the absorption and attenuation of stress wave. Second, the absorbing material should have high strength and not undergo excessive deformation under loading conditions. Table 2 illustrates the wave impedance values of several common materials. The wood structure is relatively loose and porous, and the wave impedance is closest to the optimal wave impedance (1.12×10^6 kg/m^2·s). Hence, pine pads with dimensions of 120 mm × 120 mm × 100 mm and 120 mm × 120 mm × 80 mm were selected as the boundary boundary materials in the stress wave propagation attenuation test (Figure 13). The sizes of 1#, 2#, 3#, and 4# pine pads are equal, respectively. In addition, the rubber pad and the steel pad were chosen as boundary materials of control groups for comparative analysis.

As shown in Table 3, the wave impedance values were measured. The results indicated that the wave impedance of the 4# pine pad was closest to the optimal wave impedance obtained in Section 4. In order to verify the reliability of the optimal wave impedance calculation model, a wooden pad was arranged between the rock specimen and the hydraulic jack to change the absorption boundary of stress waves. Stress wave attenuation tests were conducted by using different numbers of pine pads as boundary materials (Figure 14). During the experimental tests, the axial load was applied by the hydraulic lifting jack and then transmitted to the rock specimen through the target pads. The load was balanced by the reaction force provided by the rigid frame.

5.1. Rubber Pad and Steel Pad as Boundary Materials. When the rubber pad and steel pad were used as boundary materials, Vaseline was uniformly applied to the contact surface between the boundary material and rock specimen. An axial compressive stress (5 MPa) was applied to ensure the close contact between them. Then, a pendulum device was used to excite stress wave signals. The variation in the stress wave energy with propagation distance under the two boundary materials has been shown in Figure 15. When the rubber pad was used as the boundary absorbing material (Figure 15(a)), the wave impedance was 0.35×10^6 kg/m^2·s. R-1, R-2, R-3, R-4, and R-5 represented striking events with different initial energies. Taking event R-5 as an example, as the propagation distance increased, the energy of the waveforms received by sensors 1# to 6# was 4.82, 4.80, 4.51, 3.58, 4.01, and 5.81 (10^{-6} J), respectively. The results indicated that the energy of the signal received by sensors 1# to 4# decreased sequentially, while the energy received by sensors 5# and 6# gradually increased. The closer the sensor was to the end of rock specimen, the more disturbance it received from the superposition of reflected waves. Events R-1, R-2, R-3, and R-4 exhibited similar characteristics.

When the steel pad was used as the boundary absorbing material (Figure 15(b)), the wave impedance was 41.08×10^6 kg/m^2·s. S-1, S-2, S-3, S-4, and S-5 represented striking

Table 2: Wave impedance values of common materials.

Parameters	Rubber	Woodblock	Copper	Aluminum	Steel	Granite	Limestone	Sandstone
Wave speed (m/s)	235	3,320	4,400	6,350	5,200	4,000–6,800	3,200–5,500	3,000–4,600
Density (kg/m^3)	1,490	540	3,670	2,700	7,900	2,600–3,000	2,300–2,800	2,100–2,900
Wave impedance (10^6 kg/m^2·s)	0.35	1.79	16.15	17.15	41.08	8–20	7–19	6–13

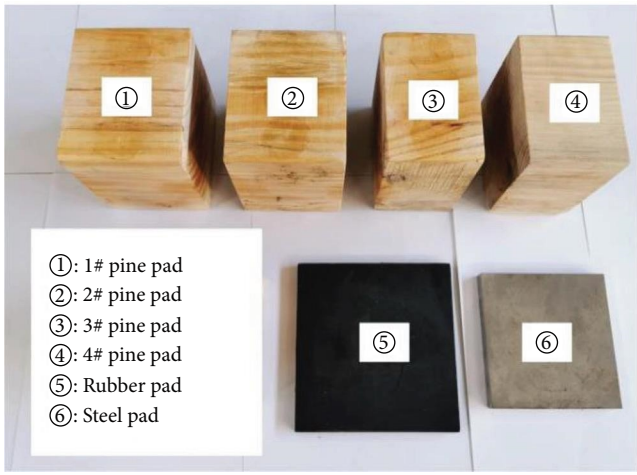

Figure 13: The boundary absorbing materials.

Table 3: The measured wave impedance values of boundary materials.

Materials	Size (mm)	Wave speed (m/s)	Density (kg/m^3)	Wave impedance (10^6 kg/m^2·s)
1# pine pad	120 × 120 × 100	5,630.02	588.80	3.31
2# pine pad	120 × 120 × 100	5,537.55	601.37	3.33
3# pine pad	120 × 120 × 80	5,075.34	435.80	2.21
4# pine pad	120 × 120 × 80	4,161.74	455.18	1.89
Rubber pad	120 × 120 × 10	235	1,490	0.35
Steel pad	120 × 120 × 10	5,200	7,900	41.08

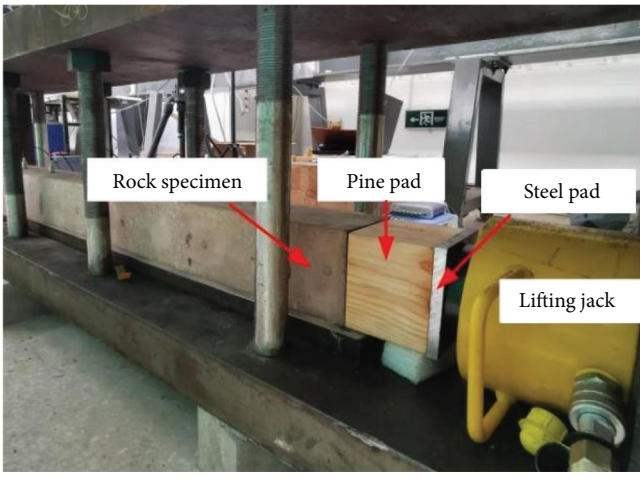

Figure 14: The arrangement of pine pad during stress wave attenuation tests.

events with different initial energies. Taking event S-5 as an example, as the propagation distance increased, the energy of the waveforms received by sensors 1# to 6# was 5.04, 4.51, 4.31, 3.56, 4.55, and 4.53 (10^{-6} J), respectively. The energy of the received signal decreased sequentially, while the energy of the signals received by sensors 5# and 6# increased. It was related to the fact that the reflected wave and the incident wave were superimposed at the 5# and 6# sensors, which increased the energy value of the received signal. According to the matching relationship of wave impedance in Figure 12, when the rubber pad and steel pad were used as boundary materials, the left-traveling reflected waves were 0.75 times and 0.7 times those of the incident wave, respectively. It indicated that when the rubber pad was used as the boundary material, the reflected wave intensity was slightly higher than that when the steel pad was used as the boundary material.

Moreover, when the rubber pad was used as the boundary material, the energy of the signal received by the 6# sensor

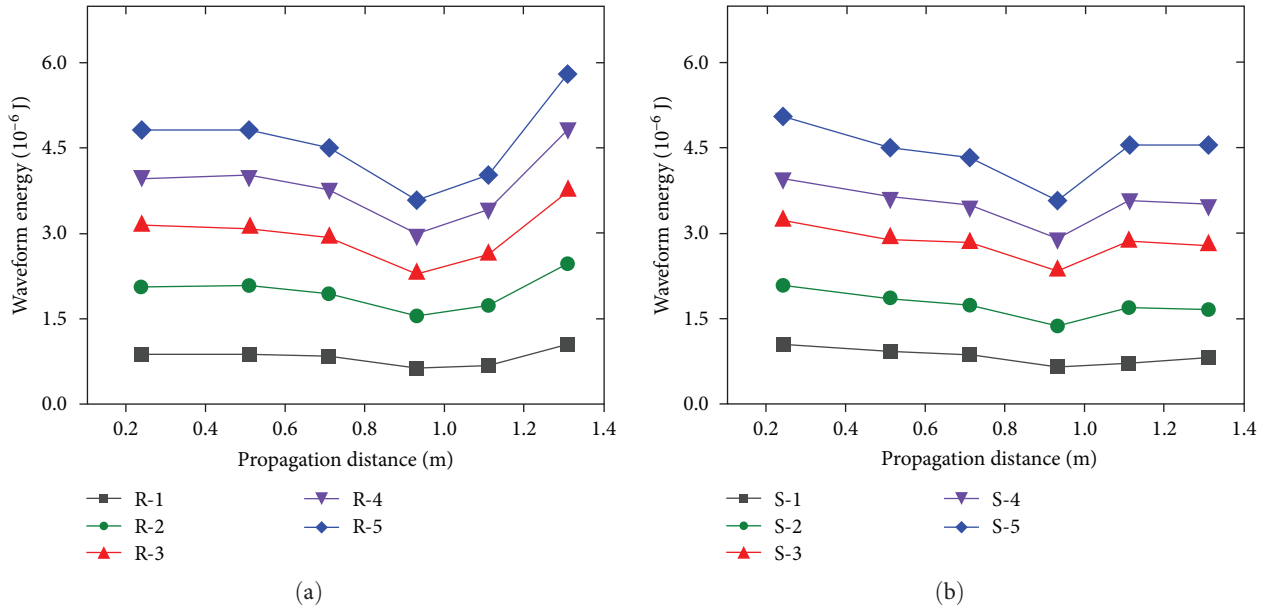

Figure 15: Variation in stress wave energy with propagation distance under different boundary conditions: (a) rubber pad and (b) steel pad.

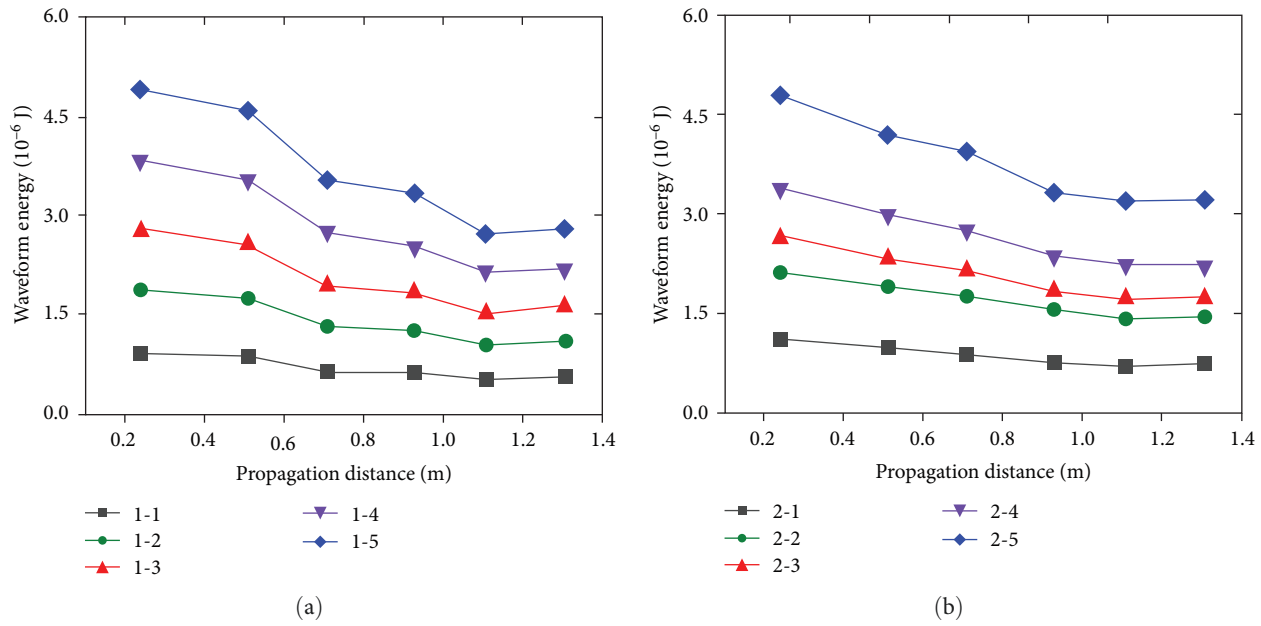

Figure 16: Variation in stress wave energy with propagation distance: (a) 1# pine pad and (b) 2# pine pad.

was greater than that received by the 5# sensor. When the steel pad was used as the boundary material, there was not a significant difference in the energy of the signal received by 5# and 6# sensors. It indicated that when the rubber pad was used as the boundary material, the intensity of the reflected waves was greater than that when the steel pad was used as the boundary material. The results confirmed the reliability of the optimal wave impedance calculation model in Section 4.

5.2. Pine Pads 1# and 2# as Boundary Materials. In order to prevent the deformation of the pine block caused by the loading cylinder of lifting jack, a steel block with dimensions of 120 mm × 120 mm × 10 mm was placed between the jack cylinder and the pine block to promote that the pine pad bears uniform force. Vaseline was uniformly applied on the contact surface between the pine pad and the rock specimen, and the equal axial stress (5 MPa) was applied to make the pine pad tightly contact the rock specimen. When the 1# pine pad was used as the boundary material, the wave impedance is considered as 3.31×10^6 kg/m^2·s. The pendulum apparatus was used to excite five waveform events with various initial energies, which were denoted as 1-1, 1-2, 1-3, 1-4, and 1-5, respectively.

The variation in the stress wave energy with propagation distance has been shown in Figure 16(a). Taking event 1-5 as

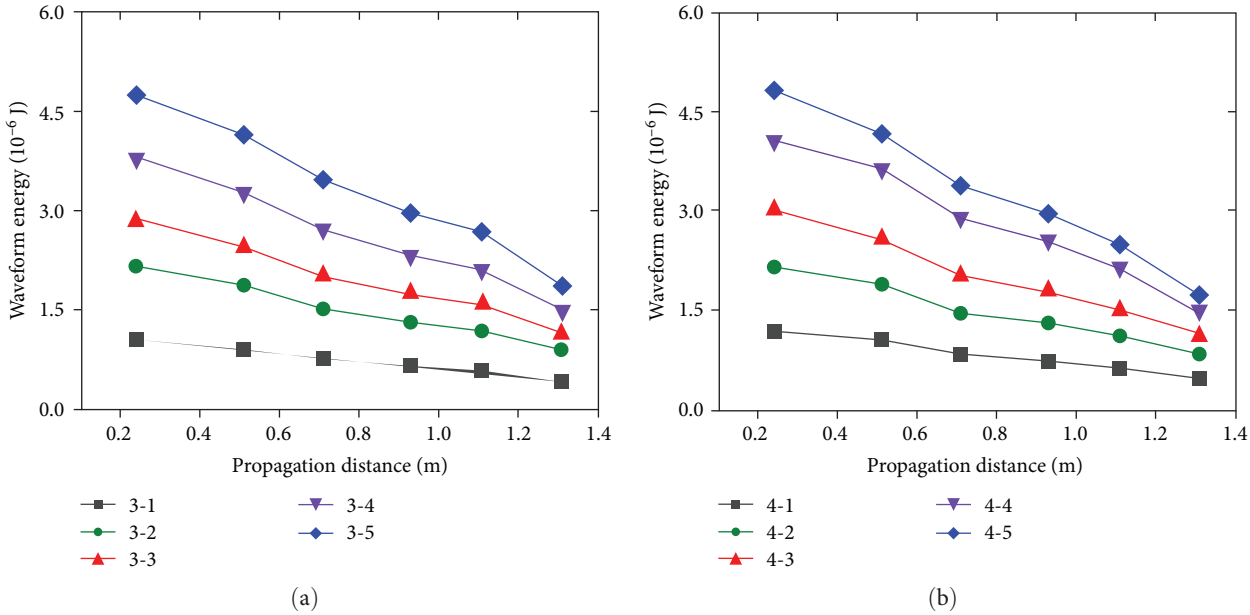

Figure 17: Variation in stress wave energy with propagation distance: (a) 3# pine pad and (b) 4# pine pad.

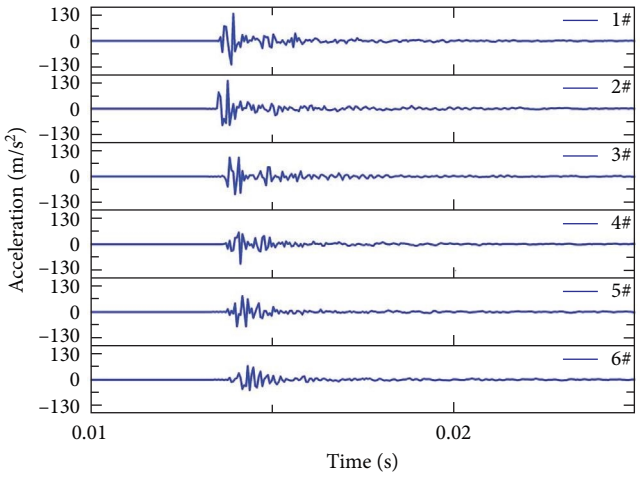

Figure 18: Time–history curves of acceleration from 1# to 6#.

an example, as the propagation distance increased, the waveform energy received by sensors 1#∼6# was 4.78, 4.18, 3.91, 3.30, 3.18, and 3.21 (10^{-6} J), respectively. The energy of the stress wave received by sensors 1#∼5# decreased sequentially, but the energy of the waveform received by sensor 6# slightly increased compared with that received by sensor 5#. The events 1-1, 1-2, 1-3, and 1-4 exhibited similar variation characteristics. According to the matching relationship of wave impedance in Figure 12, when the 1# pine pad was used as the boundary material, the reflected wave was 0.58 times the incident wave. As shown in Figure 16(a), the signal energy of sensor 6# did not increase significantly. It was related to the fact that the loose and porous structural of the pine pad significantly scattered and attenuated stress waves and decreased the reflected wave intensity during the propagation process. The variation of waveform energy in Figure 16(b) is similar to that in Figure 16(a), and the energy of stress wave decreased with increasing propagation distance.

5.3. Pine Pads 3# and 4# as Boundary Materials. When the 3# and 4# pine pads were used as the boundary absorbing materials, the wave impedance was 2.21×10^6 and 1.89×10^6 kg/m^2·s, respectively. The pendulum apparatus was used to excite waveform events with different initial energies. Figure 17 shows the variation in the stress wave energy with the propagation distance. Taking event 4-5 in Figure 17(b) as an example, as the propagation distance increased, the energy of the waveforms received by sensors 1# to 6# was 4.82, 4.17, 3.37, 2.94, 2.48, and 1.72 (10^{-6} J), respectively. The waveform energy decreased with increasing propagation distance. The events 4-1, 4-2, 4-3, and 4-4 exhibited similar variation characteristics. According to the matching relationship of wave impedance in Figure 12, when pine blocks 3# and 4# were used as the boundary material, the reflected waves were 0.42 times and 0.31 times the incident wave, respectively. When the 4# pine pad was used as the boundary material, the reflected wave intensity was weaker than that when the 3# pine pad was used as the boundary material. Due to the scattering attenuation of stress waves, the reflected wave intensity under pine boundary decreased.

The acceleration time–history curves of event 4-5 have been shown in Figure 18. As the propagation distance increased, the waveform amplitude decreased significantly. The duration of waveforms was approximately 5 ms, and there was no obvious secondary peak after the initial peak. Compared with the waveform signal acquired under free boundary conditions (Figure 9), the waveform duration of event 4-5 was reduced, and the multiple peak phenomenon did not appear. It indicated that the interference of the original waveform by the superposition of reflected waves was significantly reduced.

When the 4# pine pad was used as the boundary absorbing material, the intensity of reflected waves could be significantly reduced.

6. Prospects

The interpretation of the propagation and attenuation patterns of stress waves is a prerequisite for analyzing the dynamic response of jointed rock mass under impact load, which is critical for controlling the rock mass stability of deep underground engineering. With the continuous development of infrastructure construction and resource exploitation towards deep underground, the propagation and attenuation patterns of stress wave will be widely applied in the future.

(1) For blasting engineering, in order to reduce the disturbance of stress wave generated by the explosion to support structure and construction equipment, it is necessary to reduce the vibration intensity of stress waves over the propagation distance. The selection of appropriate absorbing materials is important for vibration isolation. In this case, experimental studies on the improvement of absorbing materials on the boundary reflection effect are helpful for optimizing wave impedance of vibration isolation materials during blasting construction.

(2) For tunnel engineering, there are often rock mass structures that alternate between soft and hard. When stress waves propagate from soft (or hard) to hard (or soft) rock masses, the wave impedance and attenuation patterns are significantly different. The rock mass in front of tunnel face can be estimated according to the stress wave propagation and attenuation patterns. In this case, the experimental test apparatus and transmission and reflection models can be used for exploring the propagation and attenuation characteristics of stress waves by simulating various rock mass combinations that alternate between soft and hard.

(3) For mining engineering, the reliable classification of potential risk zones requires accurate interpretation of stress waves excited by rock bursts. However, when the stress waves propagate from the occurrence location to the monitoring location, they have been reflected and attenuated by the jointed rock masses. The stress wave monitored by the microseismic system cannot be directly used to determine the risk level of rock burst. In this case, the accurate interpretation of the attenuation patterns and reflection effects of stress waves is important for inverting the occurrence location and energy level of rock bursts.

7. Conclusions

In the present study, a calculation method for the optimal wave impedance of boundary materials was proposed based on the transmission and reflection principle of stress waves at the interfaces of various media. The optimal wave impedance value of the boundary material has been obtained based on the calculation method. The stress wave propagation test apparatus was developed to study the improvement effect of absorbing materials on the boundary reflection effect. Stress wave propagation attenuation studies in the complete red sandstone samples were carried out by setting various boundary absorbing materials. From the present study, the following conclusions can be drawn:

(1) The waveform signal received by the accelerometer has obvious multiple peak phenomenon, and the waveform data cannot accurately reflect the propagation and attenuation characteristics of stress waves in rock masses. It is necessary to set up reasonable absorbing materials to improve the boundary reflection effect.

(2) Based on the transmission and reflection principle of stress waves at the interfaces of different media, a theoretical method for the optimal wave impedance of various boundary materials was proposed to calculate the optimal wave impedance of boundary absorbing material $Z_{op} = 1.12 \times 10^6\ \mathrm{kg/m^2 \cdot s}$.

(3) Compared with rubber and steel pads, the pine block significantly improved the boundary reflection effect of stress wave propagation. It is related to the fact that the loose and porous structure of pine pads significantly scattered and attenuated stress waves and decreased the reflected wave intensity during the propagation process.

(4) When the 4# pine block is used as the boundary material, the measured wave impedance is $1.89 \times 10^6\ \mathrm{kg/m^2 \cdot s}$. The reflection effect is the weakest, and the reflected wave is 0.31 times the incident wave. The 4# pine pad has the best suppression on the reflection effect of stress waves.

Data Availability

All data included in this study are available upon request by contact with the corresponding author.

Conflicts of Interest

The authors declare that they have no known competing financial interests or personal relationships that could have appeared to influence the work reported in this paper.

Authors' Contributions

Jian Wu was responsible for conceptualization, investigation, writing—reviewing, and editing. Yan-Tang Gao was responsible for validation, supervision, and resources. Shao-Hui Tang was responsible for methodology, investigation, writing the original draft, and visualization. Zhi-Quan Zeng was responsible for investigation and data curation. Ning Miao was responsible for formal analysis and validation. Yun-Zhi Zhong was responsible for formal analysis and data curation.

Lei Huang was responsible for supervision and data curation. Quan-Sheng Liu was responsible for methodology, validation, supervision, and resources.

Acknowledgments

The support was provided by the National Natural Science Foundation of Youth Fund Project of China (grant no. 52308415), China Postdoctoral Science Foundation on the 74th grant program (grant no. 2023M742713), and Fellowship of China Postdoctoral Science Foundation (grant no. 2022TQ0241).

References

[1] J. Wang, G. Chen, Y. Xiao, S. Li, Y. Chen, and Z. Qiao, "Effect of structural planes on rockburst distribution: case study of a deep tunnel in Southwest China," *Engineering Geology*, vol. 292, Article ID 106250, 2021.

[2] Y. Zhao, T. Yang, H. Liu et al., "A path for evaluating the mechanical response of rock masses based on deep mining-induced microseismic data: a case study," *Tunnelling and Underground Space Technology*, vol. 115, Article ID 104025, 2021.

[3] M. Askaripour, A. Saeidi, A. Rouleau, and P. Mercier-Langevin, "Rockburst in underground excavations: a review of mechanism, classification, and prediction methods," *Underground Space*, vol. 7, no. 4, pp. 577–607, 2022.

[4] W. Niu, X.-T. Feng, G. Feng et al., "Selection and characterization of microseismic information about rock mass failure for rockburst warning in a deep tunnel," *Engineering Failure Analysis*, vol. 131, Article ID 105910, 2022.

[5] J. Dai, F. Gong, and L. Xu, "Rockburst criterion and evaluation method for potential rockburst pit depth considering excavation damage effect," *Journal of Rock Mechanics and Geotechnical Engineering*, vol. 2023, pp. 1–18, 2023.

[6] F. Gong, J. Dai, and L. Xu, "A strength-stress coupling criterion for rockburst: inspirations from 1114 rockburst cases in 197 underground rock projects," *Tunnelling and Underground Space Technology*, vol. 142, Article ID 105396, 2023.

[7] M. He, M. Ding, Z. Yuan, J. Zhao, B. Luo, and X. Ma, "Numerical simulation of rock bursts triggered by blasting disturbance for deep-buried tunnels in jointed rock masses," *Computers and Geotechnics*, vol. 161, Article ID 105609, 2023.

[8] Q. Zhang, X.-P. Zhang, Q. Liu, J. Chi, and J. Qiu, "Microseismic characteristic and development mechanism of fault-slip rockburst in a deep-buried TBM excavated tunnel: a case study," *Tunnelling and Underground Space Technology*, vol. 142, Article ID 105451, 2023.

[9] Q. Zhang, X.-P. Zhang, Q. Liu, J. Qiu, and J. Wu, "Rockburst prediction and prevention in a deep-buried tunnel excavated by drilling and blasting: a case study," *Engineering Geology*, vol. 330, Article ID 107404, 2024.

[10] L. F. Trivino and B. Mohanty, "Assessment of crack initiation and propagation in rock from explosion-induced stress waves and gas expansion by cross-hole seismometry and FEM–DEM method," *International Journal of Rock Mechanics and Mining Sciences*, vol. 77, pp. 287–299, 2015.

[11] X. Sun, H. Xu, M. He, and F. Zhang, "Experimental investigation of the occurrence of rockburst in a rock specimen through infrared thermography and acoustic emission," *International Journal of Rock Mechanics and Mining Sciences*, vol. 93, pp. 250–259, 2017.

[12] J. Deng, N. S. Kanwar, M. D. Pandey, and W.-C. Xie, "Dynamic buckling mechanism of pillar rockbursts induced by stress waves," *Journal of Rock Mechanics and Geotechnical Engineering*, vol. 11, no. 5, pp. 944–953, 2019.

[13] N. W. Xu, T. B. Li, F. Dai, B. Li, Y. G. Zhu, and D. S. Yang, "Microseismic monitoring and stability evaluation for the large scale underground caverns at the Houziyan hydropower station in Southwest China," *Engineering Geology*, vol. 188, pp. 48–67, 2015.

[14] X.-J. Hao, X.-T. Feng, C.-X. Yang, Q. Jiang, and S.-J. Li, "Analysis of EDZ development of columnar jointed rock mass in the Baihetan diversion tunnel," *Rock Mechanics and Rock Engineering*, vol. 49, no. 4, pp. 1289–1312, 2016.

[15] A. Li, N. Xu, F. Dai, G. Gu, Z. Hu, and Y. Liu, "Stability analysis and failure mechanism of the steeply inclined bedded rock masses surrounding a large underground opening," *Tunnelling and Underground Space Technology*, vol. 77, pp. 45–58, 2018.

[16] L. F. Fan, X. F. Zhou, Z. J. Wu, and L. J. Wang, "Investigation of stress wave induced cracking behavior of underground rock mass by the numerical manifold method," *Tunnelling and Underground Space Technology*, vol. 92, Article ID 103032, 2019.

[17] S. He, T. Chen, I. Vennes et al., "Dynamic modelling of seismic wave propagation due to a remote seismic source: a case study," *Rock Mechanics and Rock Engineering*, vol. 53, no. 11, pp. 5177–5201, 2020.

[18] Z. Yao, Y. Fang, R. Zhang et al., "The mechanism of stick-slip as a rockburst source in jointed rockmass: an experimental study," *Rock Mechanics and Rock Engineering*, vol. 56, no. 5, pp. 3573–3593, 2023.

[19] J. Hu, H. Pan, L. Li et al., "Experimental and numerical study of joint persistence effect on the non-persistent jointed rock mass' tension failure behavior," *Rock Mechanics and Rock Engineering*, vol. 56, no. 12, pp. 9121–9134, 2023.

[20] Z. Yao, Y. Fang, T. Yu et al., "Dynamic failure mechanism of tunnel under rapid unloading in jointed rockmass: a case study," *Engineering Failure Analysis*, vol. 141, Article ID 106634, 2022.

[21] S.-M. Wang, Y.-S. Liu, K. Du, and J. Zhou, "Dynamic failure properties of sandstone under radial gradient stress and cyclical impact loading," *Frontiers in Earth Science*, vol. 7, no. 251, pp. 1–10, 2019.

[22] X. Huang, S. Qi, S. Guo, and W. Dong, "Experimental study of ultrasonic waves propagating through a rock mass with a single joint and multiple parallel joints," *Rock Mechanics and Rock Engineering*, vol. 47, no. 2, pp. 549–559, 2014.

[23] W. Wu, H. Li, and J. Zhao, "Dynamic responses of non-welded and welded rock fractures and implications for P-wave attenuation in a rock mass," *International Journal of Rock Mechanics and Mining Sciences*, vol. 77, pp. 174–181, 2015.

[24] S.-M. Wang, J. Zhou, C.-Q. Li, D. J. Armaghani, X.-B. Li, and H. S. Mitri, "Rockburst prediction in hard rock mines developing bagging and boosting tree-based ensemble techniques," *Journal of Central South University*, vol. 28, no. 2, pp. 527–542, 2021.

[25] Z. Han, D. Li, T. Zhou, Q. Zhu, and P. G. Ranjith, "Experimental study of stress wave propagation and energy characteristics across rock specimens containing cemented mortar joint with various thicknesses," *International Journal of Rock Mechanics and Mining Sciences*, vol. 131, Article ID 104352, 2020.

[26] S. Y. Fu, H. B. Li, L. W. Liu, D. Wu, and B. Wang, "Effect of intermittent joint distribution on the mechanical and acoustic

behavior of rock masses," *Journal of Rock Mechanics and Geotechnical Engineering*, vol. 15, pp. 1–14, 2023.

[27] M. He, T. Cheng, Y. Qiao, and H. Li, "A review of rockburst: experiments, theories, and simulations," *Journal of Rock Mechanics and Geotechnical Engineering*, vol. 15, no. 5, pp. 1312–1353, 2023.

[28] Q. Zhang, X. P. Zhang, Q. S. Liu, Y. C. Pan, J. J. Chi, and J. B. Qiu, "Microseismic monitoring and rockburst characteristics in a deep-buried tunnel excavated by TBM," *Rock Mechanics and Rock Engineering*, vol. 56, pp. 1–14, 2023.

[29] Q. Zhang, C.-C. Ma, X.-P. Zhang, Q. Liu, J. Qiu, and D. Liu, "Comparison of spatio-temporal characteristic of microseismic events in deep-buried tunnels with two excavation methods," *Bulletin of Engineering Geology and the Environment*, vol. 83, no. 3, pp. 1–12, 2024.

[30] S.-M. Wang, J.-Q. Wang, X.-R. Xiong, Z.-H. Chen, Y.-L. Gui, and J. Zhou, "Effect of oblique incident wave perturbation on rock spalling: an insight from DEM modelling," *Journal of Central South University*, vol. 30, no. 6, pp. 1981–1992, 2023.

[31] S.-Q. Yang, P.-F. Yin, Y.-C. Zhang et al., "Failure behavior and crack evolution mechanism of a non-persistent jointed rock mass containing a circular hole," *International Journal of Rock Mechanics and Mining Sciences*, vol. 114, pp. 101–121, 2019.

[32] M. Liu, R. Bi, X. Luo, and K. Du, "Natural joint effect on mechanical characteristics and fracture evolution of in-site rocks under uniaxial compression," *Engineering Failure Analysis*, vol. 157, Article ID 107880, 2024.

[33] C. Delle Piane, J. Sarout, C. Madonna, E. H. Saenger, D. N. Dewhurst, and M. Raven, "Frequency-dependent seismic attenuation in shales: experimental results and theoretical analysis," *Geophysical Journal International*, vol. 198, no. 1, pp. 504–515, 2014.

[34] B. Yan, P. Wang, F. Ren, Q. Guo, and M. Cai, "A review of mechanical properties and constitutive theory of rock mass anisotropy," *Arabian Journal of Geosciences*, vol. 13, no. 12, pp. 1–16, 2020.

[35] X. Bao, J. Guo, Y. Liu et al., "Damage characteristics and laws of micro-crack of underwater electric pulse fracturing coal-rock mass," *Theoretical and Applied Fracture Mechanics*, vol. 111, Article ID 102853, 2021.

[36] R. Lan, Z. Wang, J. Lu, Z. Zhou, L. Chen, and S. Gao, "The influence of the number of free surfaces on the energy distribution and attenuation law of blasting vibration signals from peripheral holes: field experiment and simulation," *Frontiers in Earth Science*, vol. 11, 2023.

[37] R. Cheng, W. Chen, H. Hao, and J. Li, "Effect of internal explosion on tunnel secondary and adjacent structures: a review," *Tunnelling and Underground Space Technology*, vol. 126, Article ID 104536, 2022.

[38] X. Chen and Z. Xu, "The ultrasonic P-wave velocity-stress relationship of rocks and its application," *Bulletin of Engineering Geology and the Environment*, vol. 76, no. 2, pp. 661–669, 2017.

[39] L. Weng, Q.-H. Wu, Y.-L. Zhao, and S.-M. Wang, "Dynamic response and failure of rock in initial gradient stress field under stress wave loading," *Journal of Central South University*, vol. 27, no. 3, pp. 963–972, 2020.

[40] J. Wu, Q. Liu, X. Zhang et al., "Attenuation characteristics of impact-induced seismic wave in deep tunnels: an in situ investigation based on pendulum impact test," *Journal of Rock Mechanics and Geotechnical Engineering*, vol. 14, no. 2, pp. 494–504, 2022.

[41] C.-P. Lu, Y. Liu, N. Zhang, T.-B. Zhao, and H.-Y. Wang, "In-situ and experimental investigations of rockburst precursor and prevention induced by fault slip," *International Journal of Rock Mechanics and Mining Sciences*, vol. 108, pp. 86–95, 2018.

[42] H. Krietsch, V. Gischig, K. Evans et al., "Stress measurements for an in situ stimulation experiment in crystalline rock: integration of induced seismicity, stress relief and hydraulic methods," *Rock Mechanics and Rock Engineering*, vol. 52, no. 2, pp. 517–542, 2019.

[43] M. Zhang, S. Liu, and H. Shimada, "Regional hazard prediction of rock bursts using microseismic energy attenuation tomography in deep mining," *Natural Hazards*, vol. 93, no. 3, pp. 1359–1378, 2018.

[44] N. Jiang, C. Zhou, S. Lu, and Z. Zhang, "Propagation and prediction of blasting vibration on slope in an open pit during underground mining," *Tunnelling and Underground Space Technology*, vol. 70, pp. 409–421, 2017.

[45] Q. Bai, M. Tibbo, M. H. B. Nasseri, and R. P. Young, "True triaxial experimental investigation of rock response around the mine-by tunnel under an in situ 3D stress path," *Rock Mechanics and Rock Engineering*, vol. 52, no. 10, pp. 3971–3986, 2019.

[46] Q. S. Liu, J. Wu, X. P. Zhang et al., "Microseismic monitoring to characterize structure-type rockbursts: a case study of a TBM-excavated tunnel," *Rock Mechanics and Rock Engineering*, vol. 53, no. 7, pp. 2995–3013, 2020.

[47] C. Kurtuluş, M. Üçkardeş, U. Sarı, and Ş Onur Güner, "Experimental studies in wave propagation across a jointed rock mass," *Bulletin of Engineering Geology and the Environment*, vol. 71, no. 2, pp. 231–234, 2012.

[48] Z. N. Tian, S. H. Li, and N. Xiao, "Experimental studies and numerical simulation of stress wave propagation in one-dimensional rock mass," *Chinese Journal of Geotechnical Engineering*, vol. 27, no. S1, pp. 2687–2693, 2008.

[49] Y. Zou, J. Li, and J. Zhao, "A novel experimental method to investigate the seismic response of rock joints under obliquely incident wave," *Rock Mechanics and Rock Engineering*, vol. 52, no. 9, pp. 3459–3466, 2019.

[50] T. Liu, J. Li, H. Li, X. Li, Y. Zheng, and H. Liu, "Experimental study of s-wave propagation through a filled rock joint," *Rock Mechanics and Rock Engineering*, vol. 50, no. 10, pp. 2645–2657, 2017.

[51] X. P. Li, H. Zhao, Y. Luo et al., "Experimental study of propagation and attenuation of elastic wave in deep rock mass with joints," *Chinese Journal of Rock Mechanics and Engineering*, vol. 34, no. 11, pp. pp, 2319–2326, 2015.

[52] L. Wang, *Fundamentals of Stress Waves*, National Defense Industry Press, 1st edition, 2005.

[53] L. J. Wang, L. F. Fan, and X. L. Du, "Non-attenuation behavior of stress wave propagation through a rock mass," *Rock Mechanics and Rock Engineering*, vol. 55, no. 7, pp. 3807–3815, 2022.

[54] Z. Meng and M. Qiang, "Analysis of vibration isolation effect of double-layer WIB based on wave impedance ratio," *Geotechnical and Geological Engineering*, vol. 41, no. 6, pp. 3699–3714, 2023.